Coupled electronic and nuclear dynamics at interfaces of artificial photosynthesis devices

Haas, T. de

Chapter 7: Charge Transfer-Induced Weakening of Vibronic Coupling for Single Terrylene Molecules Adsorbed onto hBN

Adsorption of a terrylene dye on charge donating defect sites in hBN weakens the vibronic intensities in the dye's fluorescence spectrum.

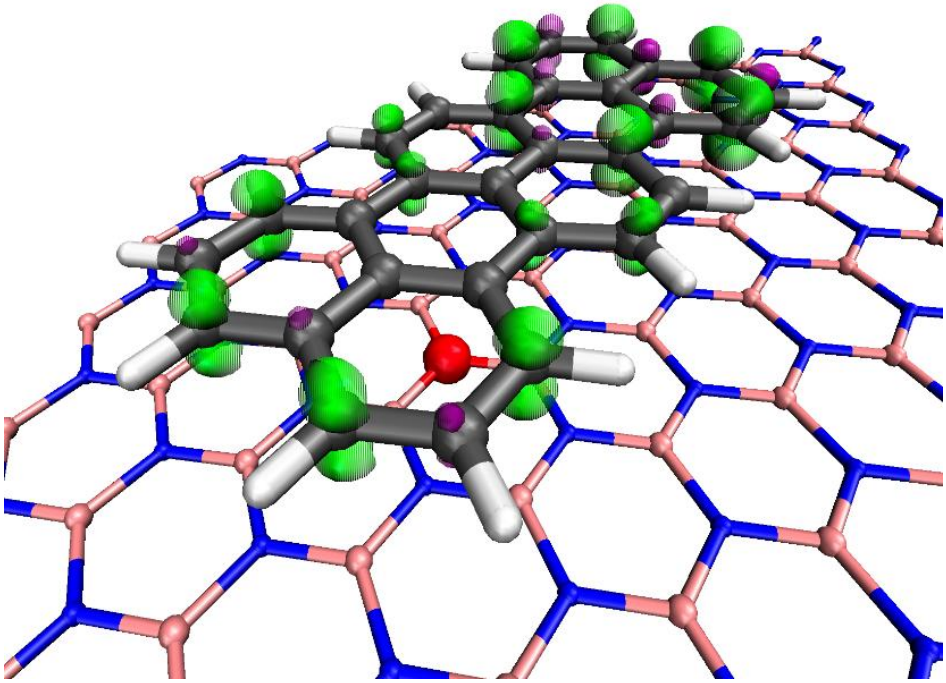

This chapter is based on:

T. de Haas*, R. Smit*, A. Tebeyani, S. Bhattacharyya, K. Watanabe, T. Taniguchi, F. Buda, M. Orrit. Charge Transfer-Induced Weakening of Vibronic Coupling for Single Terrylene Molecules Adsorbed onto Hexagonal Boron Nitride. *J. Phys. Chem. Lett.* **2025**. *16* (1), 349-356 (*contributed equally)

7.1 Abstract

Fluorescence spectra of single terrylene molecules adsorbed on hexagonal boron nitride (hBN) flakes were recorded at cryogenic temperatures. The pure electronic transitions of terrylene molecules are spread over a wavelength scale from 570 to 610 nm. Surprisingly, peaks in the vibrationally resolved fluorescence spectrum show intensity variations up to 20-fold between molecules. We find an extreme case where the Debye-Waller-Franck-Condon factor of the zero-phonon line exceeds 0.8. The vibronic intensity correlates both with the spectral position of the electronic transition and with the frequency of the longitudinal stretch mode, which varies between 243 and 257 cm^{-1}. By means of DFT calculations, we show that these observations can be explained by terrylene chemisorption on charge-donating defect sites. The electronic states of molecules at such chemisorption sites would be very attractive for the efficient emission of single photons with narrow lines and for the generation of indistinguishable photons.

7.2 Introduction

The emission of a photon by an excited molecule is generally accompanied by the release of molecular vibration quanta arising from the change in molecular geometry between the molecule's ground and excited state. The larger the change in geometry, the more pronounced are the associated vibronic bands in the fluorescence spectrum (see the theoretical discussion in section 7A.1 of the Appendix). At liquid-helium temperatures, these vibronic fluorescence lines become very sharp, a few cm^{-1} in width or less[1], and are often used as fingerprints of the single molecule under study. This so-called fluorescence line-narrowing generally works well for molecules embedded in *n*-alkane Shpol'skii matrices[2], for specific guest molecules in organic matrices[3] and, as recently demonstrated, for single terrylene molecules adsorbed on the surface of hexagonal boron nitride (hBN).[4] This latter host system is also currently scrutinized for the many single-photon emitters that it can host, with emission ranging from deep ultraviolet[5] to the near-infrared.[6] Recently, in conjunction with our work of terrylene on hBN, new insights were gathered on the potential nature of some of these emitters, namely on the potential formation of aromatic molecules at the hBN/substrate interface during high-temperature annealing.[7] The same work also summarizes the many defect structures in the hBN crystal lattice that have been proposed in the past to explain the measured emission from hBN. In addition, a recent work on hBN immersed in organic solvents showed that some solvent molecules can potentially bind to defects and display localized fluorescence, while hopping from binding site to binding site.[8] This work is particularly interesting, as it suggests that molecules can bind more strongly to specific sites on hBN.

In our previous work of single terrylene molecules on hBN, we reported that molecules with redshifted electronic transitions displayed weaker vibronic coupling, and thus show a more intense zero-phonon line in the spectrum, captured by a higher Franck-Condon-Debye-Waller factor α_{FCDW}.[4] If the interaction of the terrylene molecule with the hBN surface could be engineered so as to maximize this factor, this control method would potentially be much simpler than

current methods such as coupling a molecule to an optical cavity.[9] In this work, we examine potential origins of the weakened vibronic coupling, observed particularly for the most redshifted terrylene molecules. We perform quantum chemical calculations at the DFT level of the interaction of terrylene with a pristine hBN surface and find little change of the vibronic coupling. We then investigate several defects in the hBN lattice and find that some of them, in particular an oxygen substitution at a nitrogen site (O_N) and vacancies at the boron (V_B) or nitrogen site (V_N), can transfer charge to terrylene. Interestingly, we find that this charge transfer reduces the change in geometry between ground and excited state as compared to terrylene in vacuum and strikingly decreases the vibronic coupling of all modes simultaneously in the emission spectrum. This charge donating/accepting behaviour is also relevant to the field of dye-sensitized solar cells, where functionalized terrylenes and similar dyes have been employed for the efficient generation of photocurrents.[10,11]

7.3 Results and discussion

7.3.1 Single-Molecule Fluorescence Spectroscopy

Four examples of single-molecule fluorescence spectra obtained from four individual molecules are presented in Figure 7.1a-d and arranged by decreasing intensity of their vibronic lines. All fluorescent molecules were identified as terrylene from their ground state vibrational fingerprint, although slight differences between spectra were observed (see structure in Figure 7.1e). Most of the lines correspond to the release of a single quantum of vibration in various intramolecular modes (0-1), with their intensity related to the Franck-Condon factor of these modes (see section 7A.1 in the Appendix for a short reminder of the theory of vibronic coupling).

In addition to the intramolecular vibrational modes, we also see the phonon wing appearing most clearly between 0 and 100 cm^{-1} to the red of the 0-0 ZPL origin. The intensity of the vibronic fingerprint decreases when going from molecule A

to D, the corresponding values of the Franck-Condon-Debye-Waller factor (α_{FCDW}) being: A: 0.24, B: 0.35, C: 0.51, D: 0.80. Molecule D shows an extremely weak vibronic coupling, with a Franck-Condon-Debye-Waller factor of at least 0.80, which largely exceeds the largest ones observed for organic molecules in a matrix at low temperature. To the best of our knowledge, all factors observed so far for organic molecules were lower than 55 %.[12] Another surprising observation is that, for each molecule, the coupling strengths of all vibrational modes including lattice phonons vary in a similar way across the spectrum. An alternative formulation of this fact is that the change of geometry of some molecules upon excitation can become very small for all molecular modes simultaneously. This is surprising because, whereas we could expect a weak equilibrium shift for certain modes due to specific interaction with the substrate, we wouldn't expect this to occur simultaneously for all the modes.

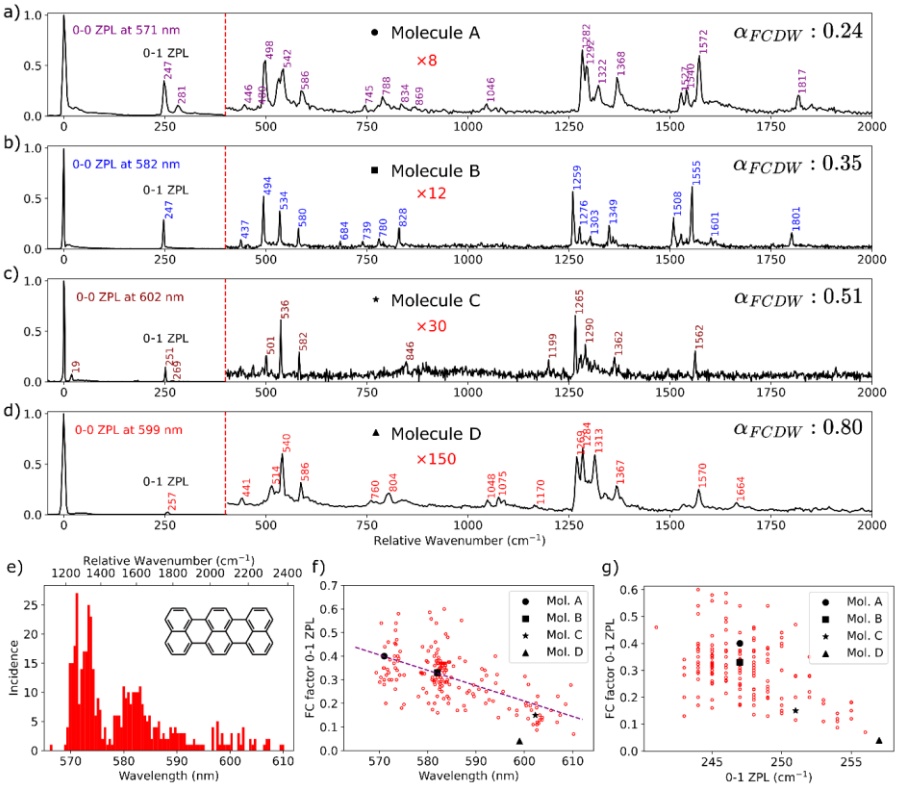

Figure 7.1. *(a)-(d) Fluorescence emission spectra from four different molecules at different wavelengths in the inhomogeneous distribution. The spectra of (A) and (D) were taken at a slightly lower resolution (600 lines/mm grating, 4 cm^{-1} resolution) as compared to (B) and (C), which were taken with a 1200 lines/mm grating (2 cm^{-1} resolution). The first three spectra show decreasing Franck-Condon factors with increase of the 0-0 zero-phonon line (ZPL) wavelength. The fourth spectrum is the most extreme case of ultra-weak vibronic coupling we could find. Note that the intensity of all vibronic lines is reduced by a factor of about 20 with respect to molecule A. Integration times were 10 s in a, 300 s in b, 150 s in c, 600 s in d. The noise in the spectra depends on integration time and mean signal intensities that varied for each molecule. Panel (e) shows the inhomogeneous distribution composed of 452 individual terrylene molecules, with the structure of terrylene in the inset. The relationship between the 0-0 ZPL and FC factor of the 0-1 ZPL is shown in panel (f), while the frequency of the vibration mode responsible for the 0-1 ZPL in relation to its FC factor is shown in panel (g). The corresponding molecules in the spectra of panel (a)-(d) are shown as black markers in the scatter plots. The purple dashed line in (f) is a guide to the eye for the trend, resulting from a linear fit to the data. We note the strong anti-correlation between the Franck-Condon factor and the frequency of the extensional mode at 250 cm^{-1} in (g). This is particularly extreme for molecule D (triangle), which is the one with the highest frequency (257 cm^{-1}) and the lowest 0-1 Franck-Condon factor (0.026) for this mode.*

Figure 7.1e presents a histogram of the 0-0 ZPL spectral positions of 452 molecules. The broad distribution in this histogram, extending over a particularly broad range (570-610 nm or more than 1000 wavenumbers), exceeds what is usually observed for terrylene embedded in molecular crystals and presents distinct maxima of around 10 cm^{-1} in width. We assign this structure in the distribution of Figure 7.1e, with maxima around 571, 582 and 600 nm, to selection

within a broad profile through resonance of vibronic lines with the excitation laser. As all molecules were excited with a fixed 532 nm laser, molecules with absorption lines at this wavelength had an increased probability to be selected in the histogram. Indeed, the relative position in wavenumber of the 0-0 zero-phonon lines (ZPLs) with respect to the laser wavelength resembles the mirror image of the vibrational spectra of Figure 7.1a-d. The large inhomogeneous broadening may be the result of significant variations in the environment around the molecule, which might be affected by parameters such as significant tensile strain[13] or the many types of (charged) defects present.[14] In addition, the annealing that we perform prior to the deposition of molecules on the hBN, may also hydroxylate parts of the hBN[15] or create wrinkles in the sheets.[16]

We now turn to the scatter plots of Figure 7.1f and 7.1g. We observe a clear correlation in Figure 7.1f between the spectral position of a molecule and the intensity of its first vibronic line at ≈ 250 cm^{-1}, corresponding to stretching of terrylene along its long axis. Redshifted molecules appear less strongly coupled to vibrations. The correlation is more pronounced in Figure 7.1g when the vibronic coupling of the longitudinal stretch mode is correlated with its frequency: molecules with high stretch frequency exhibit weaker coupling to the electronic system. This correlation reaches an extreme point for molecule D, whose FC factor for the 0-1 ZPL (0.027) is more than 10 times lower than the average over all other molecules, while its stretch mode is the one with the highest frequency at 257 cm^{-1}. As the effective mass of this skeleton mode is not likely to change much from molecule to molecule, the high frequency points to a relatively strong interaction of molecule D with the surface, which appears to change the intramolecular spring constant by about 8%.

As noted above for molecule D, we see that coupling to *all* vibrations decreases in a similar way when going from molecule A to D. Although some minor intensity changes, shifts and splitting of certain modes can be spotted, we observe no major redistribution of intensities between the main modes, so that all of them follow qualitatively the general trend observed on the 250 cm^{-1} stretch mode.

7.3.2 Quantum Chemical Calculations

Density functional theory (DFT) was employed to study physisorption of terrylene on a pristine hBN surface, and on hBN including a selection of potential lattice defects. The considered defects include a boron vacancy (V_B), a nitrogen vacancy (V_N), the boron nitride (V_{BN}) divacancy, as well as oxygen substitution at the boron (O_B) or nitrogen (O_N) centres. Indeed, as our samples were annealed in a moderate vacuum of residual air, oxygen substitution appears plausible. Although a comprehensive study of possible defects is beyond the scope of this work, these vacancies and substitutions are representative for a wider range of defects with either electron-accepting or electron-donating properties. Ground state structure optimizations and band structure calculations of the terrylene-hBN interfaces were performed at the HSE06+D3BJ DFT-level using the CP2K software package.[17–19] Calculations of the vibronic spectra were subsequently performed with FCclasses3 software using geometries, hessians and dipole moments calculated with Gaussian.[20,21] In these excited state calculations, a two-layer ONIOM(B3LYP/PM3) approach was employed, as considering the entire interface structure at the time-dependent DFT (TD-DFT) level was too computationally demanding.[22–30] Details on the computational workflow are provided in A2 and A3 of the Appendix.

Table 7.1: Adsorption energies and properties of terrylene adsorbed on different defects.*

			long-axis length (Å)			short-axis length (Å)		
	Adsorption energy (eV)	Mulliken charge on terrylene (atomic units)	Ground state	Excited state	Δx	Ground state	Excited state	Δx
vacuum	-	-	10.078	10.044	-0.034	4.839	4.883	0.044
pristine hBN	−2.44	0.02	10.089	10.054	-0.035	4.843	4.887	0.044
V_{BN}**	−2.36	0.02	-	-	-	-	-	-
V_B	−2.52	0.83	10.054	10.041	-0.013	4.829	4.854	0.023
V_N	−2.46	−0.68	10.094	10.082	-0.012	4.839	4.860	0.021
O_B**	−2.29	0.01	-	-	-	-	-	-
O_N	−3.96	−0.70	10.095	10.083	-0.012	4.839	4.860	0.021

* Note that adsorption energies and Mulliken charges are calculated at the full-DFT level, while the structural properties are calculated at the ONIOM(B3LYP/PM3) level. Δx indicates the change in axis length from the excited to the ground state.

** As the V_{BN} and O_B defects have a lower binding energy for the terrylene molecule compared to defect-free hBN, we did not further investigate the excited state geometry of terrylene on these defects.

The first two columns of Table 7.1 present physisorption energies and partial Mulliken charge accumulation on terrylene in the presence of defects, calculated at the full DFT-level. The charge analysis has also been performed using Hirshfeld and Intrinsic Orbital Analysis charges, which show the same trend and are provided in the Appendix, Table 7A.2.[31] The physisorption energy of terrylene on a perfect monolayer of hBN was found to be –2.44 eV, compared to terrylene and hBN in vacuum. This adsorption energy follows the trend reported in literature of increasing adsorption energy with increasing molecule size for polycyclic aromatic hydrocarbons (PAH's) on hBN.[32] Defect site binding energies were established by comparing adsorption energies on defects with the adsorption energy on the defect-free lattice. It was found that the V_{BN} divacancy and the O_B defects bind the molecule less strongly than pristine hBN, with 0.08 and 0.15 eV, respectively. It is therefore unlikely that the terrylene molecule would be localized on these specific defects. Contrarily, the adsorption energy in

the presence of the V_N and V_B vacancies is slightly higher (by 0.02 and 0.08 eV) than the defect-free case, and specifically for the O_N defect the binding is much stronger (by 1.52 eV). Notably, this latter defect has also been proposed as a source for specific features observed in X-ray spectroscopy.[33] The reported partial Mulliken charges reveal that the three terrylene adsorbing defects (V_N, V_B, O_N) donate a considerable amount of electron (V_N, O_N) or hole (V_B) density to terrylene. This type of charge transfer has been reported before in GGA-based DFT studies on hBN-graphene heterostructures.[34] Because of the charge transfer, we observe significant changes in the extent to which terrylene elongates or contracts upon excitation from the ground to the excited state. For instance, in the defect-free hBN, the long-axis contraction in the excited state is −0.035 Å, whereas in the presence of the O_N defect, this contraction is reduced to only −0.012 Å (see Table 7.1). Therefore, one can expect the intensity of vibrational modes coupled to the electronic transition to be affected considerably in the fluorescence spectrum.

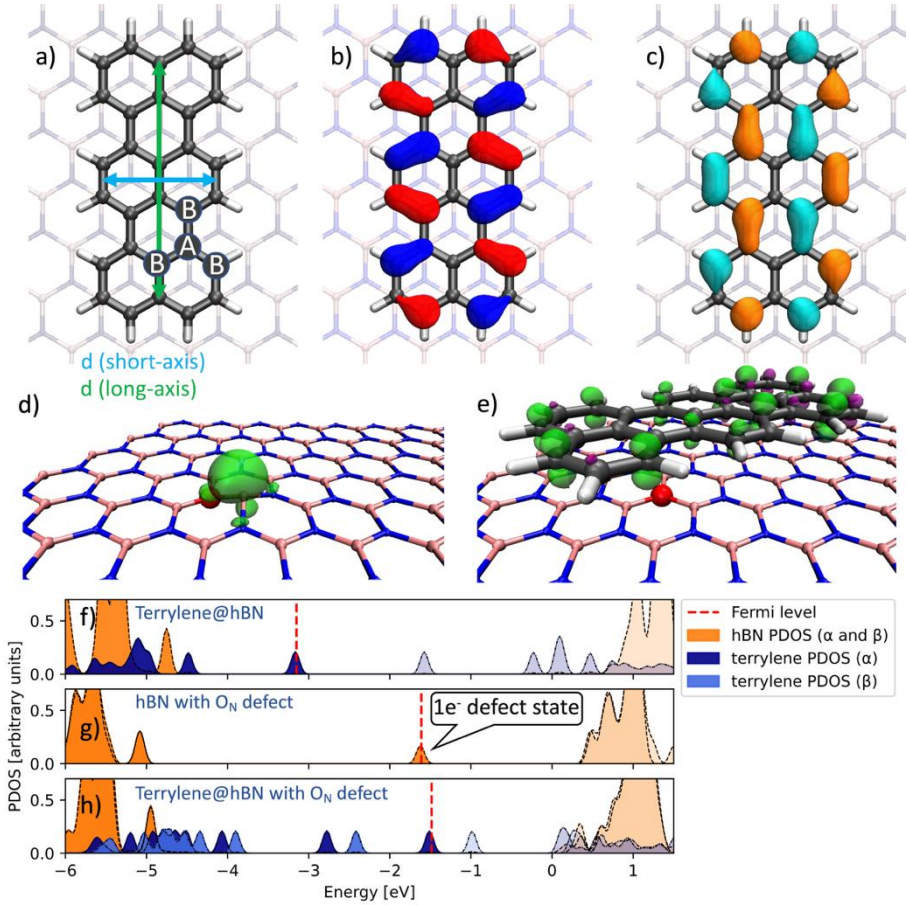

Figure 7.2. *(a)-(c) terrylene molecules adsorbed on a single monolayer of pristine hBN. a) shows the longitudinal (green) and short (blue) axis, while the HOMO and LUMO are shown in b) and c), with the isosurfaces plotted at 0.03 a.u. The carbon atoms of the graphene A- and B-sublattices of terrylene are depicted with insets in (a). (d) and (e) show the spin density on the O_N chemisorption site before and after binding of terrylene with an isosurface plotted at 0.005 a.u. Projected density of states (PDOS) of terrylene adsorbed on pristine hBN (f), of hBN with the O_N defect (g) and of terrylene adsorbed on hBN with the O_N defect (h). The PDOS were computed in CP2K at the HSE06+D3(BJ)-level and include a Gaussian broadening of 0.05 eV. Bands with transparent colors correspond to unoccupied levels. The α and β bands for hBN with the O_N defect in (g) and (h)*

largely overlap and are depicted in the same color (orange). However, it should be noted that the defect state in panel (g) is singly occupied.

Figure 7.2a shows the optimized geometry of terrylene on the hBN single-layer lattice. The two structures are nearly commensurate. The terrylene carbon atoms of the graphene A-sublattice are found to reside on top of monolayer boron atoms, whereas the terrylene carbon atoms of the B-sublattice are placed over the centers of the $(BN)_3$ hexagons (A- and B-sublattices are indicated in Figure 7.2a). The hBN nitrogens are thus placed underneath the centers of the terrylene aromatic rings. Previous theoretical works have also found this configuration to be most stable for similar PAH's on hBN.[32,35] Our TD-DFT calculations show that the experimentally observed fluorescence around 600 nm is associated with the electronic transition that involves predominantly (>70%) the HOMO and LUMO orbitals. Figure 7.2b and 7.2c present the HOMO and LUMO orbitals of the terrylene molecule on the hBN surface. Both orbitals are localized on the terrylene molecule and do not hybridize with hBN electronic states. This is in line with Figure 7.2f, which shows that the frontier orbitals of terrylene are found to reside completely isolated within the hBN bandgap. The calculated bandgap of ~5.7 eV is similar to previous studies reporting hBN bandgaps of ~6 eV.[35,36] The shapes of the HOMO and LUMO orbitals provide a physical interpretation for the observed short-axis elongation and long-axis contraction when terrylene is excited from the ground to the excited state, as electron density is transferred from bonding orbitals along the short-axis to bonding orbitals along the long-axis. Similarly, one can expect that populating the LUMO orbital may affect the spectral position of the long-axis vibration observed around ≈250 cm^{-1}.

For the remainder of this discussion, we focus on the terrylene interaction with the O_N defect, as binding to this defect was found to be particularly strong. Figure 7.2d shows the spin density at the O_N defect site. Interestingly, the excess electron is localized almost entirely on the lone-pair of the boron atom adjacent to the

introduced oxygen atom, resulting in an out-of-plane distortion of the boron atom. Figure 7.2g shows that the introduced defect state is localized within the hBN bandgap, at a similar energy as the terrylene LUMO orbital. Upon chemisorption of terrylene, the excess electron is transferred to the terrylene as is made apparent by the spin density in Figure 7.2e and the PDOS plot in Figure 7.2h. Once the excess electron has transferred to terrylene, the hBN relaxes again to its planar structure. A similar electron donor state is introduced by the V_N vacancy, which is shown in the Appendix, Figure 7A.2. We note that the terrylene HOMO-LUMO gap decreases upon charge transfer. This aligns with the redshift of the 0-0 ZPL that was observed for specific terrylene molecules in the single molecule fluorescence experiments. In contrast to the O_N and V_N cases, the V_B vacancy introduces an acceptor state close to the valence band. In this case, it is the terrylene molecule that donates charge to the hBN surface, rather than the opposite (see Appendix, Figure 7A.3). Despite considerable charge transfer at all these chemisorption sites, no single isolated covalent bond is formed between the adsorbate and adsorber. Only a *ca.* 0.2 Å shortening of the terrylene-hBN distance is observed in the case of chemisorption on the O_N and V_N defects (see Appendix, Table 7A.3).

In addition to the geometry optimizations, PBE-DFT-based molecular dynamics simulations were carried out to gain insights into the diffusive behaviour of terrylene on pristine hBN. The optimized structure was used as input for a 5 ps equilibration run at 300 K. Subsequently, the system was propagated for another 5 ps in a production run. Figure 7A.4 shows three structures sampled from the MD production run trajectory at 0, 2 and 4 ps. Despite the relatively high binding energy, the MD simulations show that at 300 K, terrylene can rotate and even translate on the pristine hBN monolayer on the picosecond timescale. This corroborates our interpretation that the observed localized emission at room temperature[37] originates from terrylene chemisorbed at specific defect sites.

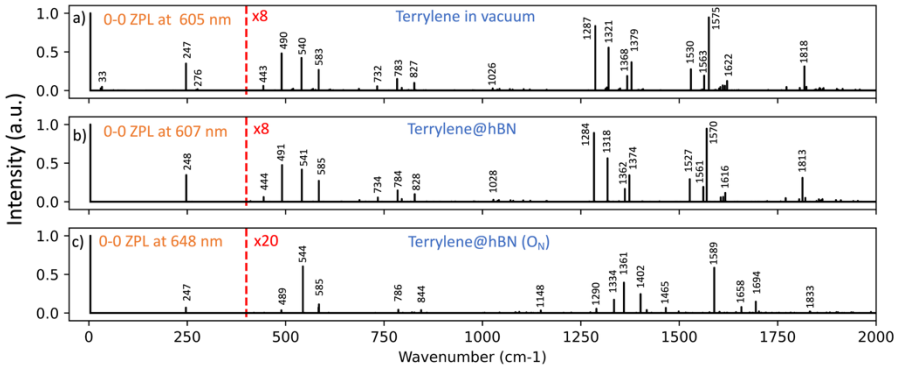

***Figure 7.3**. Computed vibrationally resolved fluorescence spectra of terrylene in vacuum (a), on hBN (b) and adsorbed onto the O_N defect (c). All spectra are shifted such that their respective 0-0 Zero Phonon Line (ZPL) is centred at 0. The spectra are corrected with a linear scaling function with parameters 0.977 and 4.132, as suggested by Palafox.[38] All intensities are scaled such that the intensity of the 0-0 ZPL equals 1. The intensities of the peaks observed above 400 cm^{-1} are multiplied by a factor 8 for a) and b) and a factor of 20 for c).*

7.3.3 Calculation of the Vibrationally Resolved Fluorescence Spectra

Figure 7.3 shows the calculated vibrationally resolved fluorescence spectra for terrylene in vacuum, terrylene on hBN and terrylene adsorbed onto the O_N defect site. Both the spectra of terrylene in vacuum and terrylene on pristine hBN match very closely the experimental spectrum reported for molecule A in Figure 7.1a. The most prominent feature in all simulated spectra is the peak observed at around 250 cm^{-1}, which originates from a stretching vibration along the terrylene longitudinal axis (Figure 7A.6, mode 11).[39,40] Other strong peaks in the spectrum are found around ~1285 and ~1570 cm^{-1} and also involve nuclear distortions in the same direction and with the same A_g symmetry (Figure 7A.6, mode 86 and mode 108). The peaks around 540 cm^{-1} are associated with a contraction along the terrylene short-axis and preserve the same A_g symmetry. Table 7A.4 in the

Appendix provides a complete assignment of the fluorescence signals with an intensity above 1% of the 0-0 ZPL intensity. Our interpretation aligns with that of Deperasińska and Kozankiewicz, and of Greiner and Sundholm.[39,40]

None of the vibrational peak intensities change significantly between the terrylene spectrum in vacuum and the terrylene spectrum on pristine hBN. We thus conclude that the observed ultra-weak vibronic coupling cannot be attributed solely to the adsorption process of terrylene on the defect-free lattice. However, both the fluorescence wavelength and intensity of features in the spectrum change drastically when terrylene is chemisorbed on the O_N defect site (or on the V_N and V_B sites, see Appendix, Figure 7A.5). The effective charge transfer and consequential structural rearrangement in the ground and excited state led to a much weaker vibronic coupling, characterized by an overall diminished intensity of all vibrational features and an increased intensity of the 0-0 ZPL. The intensity ratio of the stretching mode around 250 cm^{-1} to the ZPL decreases by a factor ≈5 when comparing the terrylene on defect-free hBN with the terrylene on the O_N defect (see tables 7A.5 and 7A.6 in Appendix). Interestingly, peaks that originate from vibrational overtones and combinations of vibrational modes are weaker than peaks that originate from a single mode in its lowest vibrational state, as demonstrated by the ~490 cm^{-1} and ~1817 cm^{-1} peaks which almost vanish in spectrum c, Figure 7.3. This diminishing of overtone peaks is also observed in the experimental spectra in Figure 7.1c and Figure 7.1d. The observation that all peaks are simultaneously diminished is explained by the fact that all visible vibrational modes have the same symmetry and involve nuclear displacements along the terrylene short and long axes (see Appendix, Figure 7A.6). The wavelength of the 0-0 ZPL shifts to the red by ~43 nm by introducing the O_N and V_N defects (see Figure 7.3 and Figure 7A.5), closely matching the experimentally observed redshift. Terrylene adsorption on the hole-donating V_B vacancy also leads to a diminished vibronic coupling, but to a much larger, *ca.* 100 nm, redshift of the 0-0 ZPL (see Figure 7A.5). Even though this redshift is larger than the experimentally observed redshift, we do not rule out the possibility of electron-

withdrawing defects affecting the fluorescence spectrum, as the too large shift could be an artifact of exaggerated charge transfer description within the ONIOM approach. In summary, the significant overall reduction of vibronic coupling, the nearly vanishing vibrational overtones, and the redshifted 0-0 ZPL observed for terrylene on charge-donating defects, strongly suggest that such a defect may be responsible for the experimentally observed large molecule-to-molecule variations.[41] In the work of Vasilev *et al*.,[42] large shifts of a 0-0 ZPL were also observed upon localized charging of a phthalocyanine molecule through deprotonation. These shifts were interpreted as an 'internal Stark effect'. In our case, the interaction of terrylene with a particular hBN defect also leads to charge transfer from the defect to the aromatic molecule, and therefore to local electric fields shifting the electronic transition. These effects are naturally included in the DFT calculations that reproduce the redshift of the 0-0 ZPL. In a similar manner, the change in vibronic coupling intensity, which we observe experimentally and confirm through DFT calculations, could be interpreted as a vibrational Stark effect, *i.e*., a change of coupling due to charge transfer-induced local fields.

7.4 Conclusion

As noted in earlier experiments,[4] the single terrylene molecules observed through fluorescence on an hBN surface don't diffuse translationally or rotationally at low temperature and even show localized emission at room temperature.[37] The latter observation is in contrast to the performed molecular dynamics simulations that show that molecules would diffuse rapidly on defect-free hBN. Moreover, many molecules display a comparatively strong redshift of their optical transition (from 570 nm to up to more than 620 nm), and considerable variation in the intensity of their vibronic structure in fluorescence. These observations point to a strong interaction of the molecule with the substrate, although the interaction is not strong enough to radically modify the chemical nature of terrylene. As Van der Waals interactions of terrylene with hBN are not strong enough to account for the

above observations, it is natural to assume that some degree of chemisorption between the molecule and the surface takes place. From quantum chemical calculations, we can select two potential candidate binding sites that are given by chemisorption to a O_N or V_N defect assisted by charge transfer from the defect to terrylene. Moreover, the binding to such defects affects the geometries of terrylene in the ground and excited states in such a way that the vibronic couplings of all modes are affected simultaneously, as observed in experiment. To experimentally investigate the possibility of specific defects to be responsible for chemisorption of terrylene, we propose experiments that involve the engineering of defects, such as oxygen-related defects created by hydrogen plasma irradiation[43] or vacancies by low-energy ion irradiation[44].

7.5 References

[1] J. Zirkelbach, M. Mirzaei, I. Deperasińska, B. Kozankiewicz, B. Gurlek, A. Shkarin, T. Utikal, S. Götzinger, V. Sandoghdar, *J. Chem. Phys.* **2022**, *156*, 104301.

[2] C. Gooijer, F. Ariese, J. W. Hofstraat, *Shpol'skii Spectroscopy and Other Site-Selection Methods. Applications in Environmental Analysis, Bioanalytical Chemistry, and Chemical Physics*, Wiley And Sons, New York, **2000**.

[3] S. Adhikari, R. Smit, M. Orrit, *J. Phys. Chem. C* **2024**, *128*, 3–18.

[4] R. Smit, A. Tebyani, J. Hameury, S. J. van der Molen, M. Orrit, *Nat. Commun.* **2023**, *14*, 7960.

[5] R. Bourrellier, S. Meuret, A. Tararan, O. Stéphan, M. Kociak, L. H. G. Tizei, A. Zobelli, *Nano Lett.* **2016**, *16*, 4317–4321.

[6] R. Camphausen, L. Marini, S. A. Tawfik, T. T. Tran, M. J. Ford, S. Palomba, *APL Photonics* **2020**, *5*, 076103.

[7] M. Neumann, X. Wei, L. Morales-Inostroza, S. Song, S.-G. Lee, K. Watanabe, T. Taniguchi, S. Götzinger, Y. H. Lee, *ACS Nano* **2023**, *17*, 11679–11691.

[8] N. Ronceray, Y. You, E. Glushkov, M. Lihter, B. Rehl, T.-H. Chen, G.-H. Nam, F. Borza, K. Watanabe, T. Taniguchi, S. Roke, A. Keerthi, J. Comtet, B. Radha, A. Radenovic, *Nat. Mater.* **2023**, *22*, 1236–1242.

[9] D. Wang, H. Kelkar, D. Martin-Cano, D. Rattenbacher, A. Shkarin, T. Utikal, S. Götzinger, V. Sandoghdar, *Nat. Phys.* **2019**, *15*, 483–489.

[10] T. Edvinsson, N. Pschirer, J. Schöneboom, F. Eickemeyer, G. Boschloo, A. Hagfeldt, *Chem. Phys.* **2009**, *357*, 124–131.

[11] A. Monti, C. F. A. Negre, V. S. Batista, L. G. C. Rego, H. J. M. de Groot, F. Buda, *J. Phys. Chem. Lett.* **2015**, *6*, 2393–2398.

[12] R. C. Schofield, P. Burdekin, A. Fasoulakis, L. Devanz, D. P. Bogusz, R. A. Hoggarth, K. D. Major, A. S. Clark, *ChemPhysChem* **2022**, *23*, e202100809.

[13] N. Mendelson, M. Doherty, M. Toth, I. Aharonovich, T. T. Tran, *Adv. Mater.* **2020**, *32*, 1908316.

[14] D. Wong, J. Velasco, L. Ju, J. Lee, S. Kahn, H.-Z. Tsai, C. Germany, T. Taniguchi, K. Watanabe, A. Zettl, F. Wang, M. F. Crommie, *Nat. Nanotechnol.* **2015**, *10*, 949–953.

[15] J. Ren, L. Stagi, P. Innocenzi, *J. Mater. Sci.* **2021**, *56*, 4053–4079.

[16] G. Zhang, Y. Chang, B. Yan, *Cryst.* **2023**, *13*, 304.
[17] J. Heyd, G. E. Scuseria, M. Ernzerhof, *J. Chem. Phys.* **2003**, *118*, 8207–8215.
[18] J. Heyd, G. E. Scuseria, *J. Chem. Phys.* **2004**, *121*, 1187–1192.
[19] T. D. Kühne, M. Iannuzzi, M. Del Ben, V. V. Rybkin, P. Seewald, F. Stein, T. Laino, R. Z. Khaliullin, O. Schütt, F. Schiffmann, D. Golze, J. Wilhelm, S. Chulkov, M. H. Bani-Hashemian, V. Weber, U. Borštnik, M. Taillefumier, A. S. Jakobovits, A. Lazzaro, H. Pabst, T. Müller, R. Schade, M. Guidon, S. Andermatt, N. Holmberg, G. K. Schenter, A. Hehn, A. Bussy, F. Belleflamme, G. Tabacchi, A. Glöß, M. Lass, I. Bethune, C. J. Mundy, C. Plessl, M. Watkins, J. VandeVondele, M. Krack, J. Hutter, *J. Chem. Phys.* **2020**, *152*, 194103.
[20] J. Cerezo, F. Santoro, *J. Comput. Chem.* **2023**, *44*, 626–643.
[21] M. J. Frisch, G. W. Trucks, H. B. Schlegel G. E. Scuseria, M. A. Robb, J. R. Cheeseman, G. Scalmani, V. Barone, G. A. Petersson, H. Nakatsuji, X. Li, M. Caricato, A. V. Marenich, J. Bloino, B. G. Janesko, R. Gomperts, B. Mennucci, Gaussian 16; Gaussian, Inc.: Wallingford, CT, 2016.
[22] S. Dapprich, I. Komaromi, K. S. Byun, K. Morokuma, M. J. Frisch, **1999**.
[23] L. W. Chung, W. M. C. Sameera, R. Ramozzi, A. J. Page, M. Hatanaka, G. P. Petrova, T. V. Harris, X. Li, Z. Ke, F. Liu, H.-B. Li, L. Ding, K. Morokuma, *Chem. Rev.* **2015**, *115*, 5678–5796.
[24] A. D. Becke, *J. Chem. Phys.* **1993**, *98*, 1372–1377.
[25] S. H. Vosko, L. Wilk, M. Nusair, *Can. J. Phys.* **1980**, *58*, 1200–1211.
[26] C. Lee, W. Yang, R. G. Parr, *Phys. Rev. B* **1988**, *37*, 785–789.
[27] P. J. Stephen, F. J. Devlin, C. F. Chabalowski, M. J. Frisch, *J. Phys. Chem.* **1994**, *98*, 11623–11627.
[28] J. J. P. Stewart, *J. Comput. Chem.* **1989**, *10*, 209–220.
[29] J. J. P. Stewart, *J. Comput. Chem.* **1989**, *10*, 221–264.
[30] J. J. P. Stewart, *J. Comput. Chem.* **1991**, *12*, 320–341.
[31] G. Knizia, *J. Chem. Theory Comput.* **2013**, *9*, 4834–4843.
[32] X. Chen, S. Jia, N. Ding, J. Shi, Z. Wang, *Environ. Sci.: Nano* **2016**, *3*, 1493–1503.
[33] N. L. McDougall, J. G. Partridge, R. J. Nicholls, S. P. Russo, D. G. McCulloch, *Phys. Rev. B* **2017**, *96*, 144106.
[34] M. K. Prasad, O. A. Al-Ani, J. P. Goss, J. D. Mar, *Phys. Rev. Materials* **2023**, *7*, 094003.
[35] G. Melani, J. P. Guerrero-Felipe, A. M. Valencia, J. Krumland, C. Cocchi, M. Iannuzzi, *Phys. Chem. Chem. Phys.* **2022**, *24*, 16671–16679.
[36] C. Elias, P. Valvin, T. Pelini, A. Summerfield, C. J. Mellor, T. S. Cheng, L. Eaves, C. T. Foxon, P. H. Beton, S. V. Novikov, B. Gil, G. Cassabois, *Nat. Commun.* **2019**, *10*, 2639.
[37] S. Han, C. Qin, Y. Song, S. Dong, Y. Lei, S. Wang, X. Su, A. Wei, X. Li, G. Zhang, R. Chen, J. Hu, L. Xiao, S. Jia, *J. Chem. Phys.* **2021**, *155*, 244301.
[38] M. A. Palafox, *Phys. Sci. Rev.* **2018**, *3*, DOI 10.1515/psr-2017-0184.
[39] I. Deperasińska, B. Kozankiewicz, *Chem. Phys. Lett.* **2017**, *684*, 208–211.
[40] J. Greiner, D. Sundholm, *Phys. Chem. Chem. Phys.* **2020**, *22*, 2379–2385.
[41] K. Vasilev, B. Doppagne, T. Neuman, A. Rosławska, H. Bulou, A. Boeglin, F. Scheurer, G. Schull, *Nat. Commun.* **2022**, *13*, 677.
[42] K. Vasilev, B. Doppagne, T. Neuman, A. Rosławska, H. Bulou, A. Boeglin, F. Scheurer, G. Schull, *Nat. Commun.* **2022**, *13*, 677.
[43] Y. Xiao, H. Yu, H. Wang, X. Zhu, L. Chen, W. Gao, C. Liu, H. Yin, *Appl. Surf. Sci.* **2022**, *593*, 153386.
[44] M. Längle, B. M. Mayer, J. Madsen, D. Propst, A. Bo, C. Kofler, V. Hana, C. Mangler, T. Susi, J. Kotakoski, *arXiv*, **2024**, DOI: 10.48550/arXiv.2404.07166.

7A. Appendix

7A.1 Theory of vibronic coupling

We will briefly remind the reader of vibronic coupling and of its importance in chemical analysis and cryogenic single-molecule spectroscopy. As a simplifying hypothesis, we assume that only the minimum of the harmonic potential of each mode changes slightly upon an electronic transition from the excited to the ground electronic state, *i.e.* that the vibration frequency does not change. This approximation, called linear vibronic coupling, works well for most intramolecular vibration modes of aromatic molecules. Figure 7A.1a shows a cut of the potential hypersurfaces of the ground (S_0) and excited (S_1) state along the vibrational coordinate, x, of a single vibration mode. At liquid-helium temperature, fluorescence proceeds from the lowest vibronic state of the excited state S_1 to vibrationally excited levels of the ground state S_0 (see downward arrows in Figure 7A.1a). The corresponding lines in the fluorescence spectrum will be the purely electronic transition (hereafter called 0-0 zero-phonon line and denoted with a yellow arrow, or ZPL for short) and a series of vibronic components at longer wavelengths corresponding to the creation of dominantly 1, 2 or more quanta of vibration (arrows of respectively orange and red color).

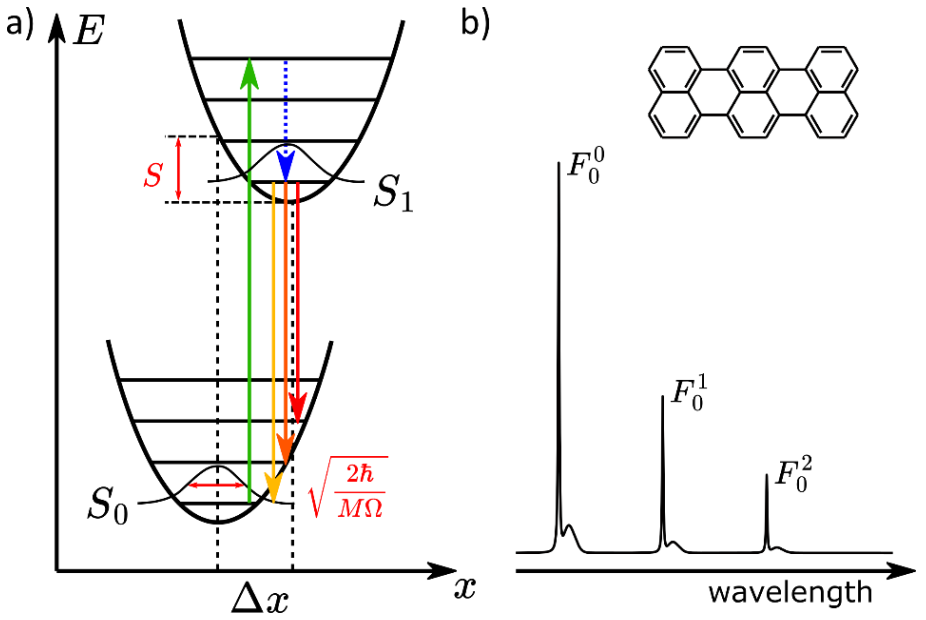

***Figure 7A.1**: a) Schematic harmonic potentials of the ground and excited molecular electronic states, with associated vibrational levels for a single vibration mode (mode coordinate x) under the linear coupling approximation. The figure displays some quantities used in the text of section 7A.1. The intensity of vibronic bands scales as the overlap of nuclear vibrational wavefunctions and for the 0-1 emission (orange arrow) it increases quadratically with the coordinate displacement Δx, as long as it remains small. The shift Δx can be alternatively represented by the associated energy stabilization S upon relaxation of the ground state geometry in the excited state. b) Schematic structure of terrylene together with a schematic representation of typical emission lines (downward arrows in (a)) whose relative intensities are associated with Franck-Condon factors. The vibronic bands are usually observed to be coupled to phonons by the presence of a phonon sideband, appearing on the red side of each narrow line.*

The intensity of the vibronic lines is given by the overlap of nuclear wavefunctions called Franck-Condon factors. For linear coupling to one mode, the Franck-Condon factor F_0^n for the release of n quanta has a simple expression:

$$F_0^n = \frac{\xi^{2n}}{n!} e^{-\xi^2}, F_0^0 = e^{-\xi^2},$$

with

$$\xi = \frac{\Delta x}{\sigma_x} \quad ,$$

where Δx is the position shift of the mode upon electronic excitation, and $\sigma_x = \sqrt{\frac{2\hbar}{M\Omega}}$ characterizes the coordinate's quantum spread in the ground state of the mode, with effective mass M and frequency Ω. The position shift of the mode is often characterized by the ratio of the reorganization energy or Stokes loss S (see Figure 7A.1) to the vibrational quantum $\hbar\Omega$:

$$\xi^2 = \frac{S}{\hbar\Omega} \quad .$$

For several independent modes, and assuming that the mode decomposition does not change upon excitation, the Franck-Condon factors are simply the products of factors for each mode i. The strength of the 0-0 transition is then $\alpha_{\mathrm{FC}} = \exp(-\xi^2)$,

with

$$\xi^2 = \sum_i \frac{S_i}{\hbar\Omega_i} \quad .$$

It is usual and convenient to distinguish lattice phonons from intramolecular vibrations. For lattice phonons, the above analysis leads to a ratio of the pure electronic transition intensity I_{ZPL} compared to that I_{PW} of the phonon wing $\alpha_{\mathrm{DW}} = I_{\mathrm{ZPL}}/(I_{\mathrm{ZPL}} + I_{\mathrm{PW}})$ called the Debye-Waller factor. The strength of the combined purely electronic transition free from any phonon or intramolecular vibration, the 0-0 ZPL, is thus a combined Franck-Condon-Debye-Waller factor α_{FCDW}:

$$\alpha_{\mathrm{FCDW}} = \alpha_{\mathrm{FC}}\alpha_{\mathrm{DW}}.$$

In the case of many weakly coupled modes, this factor can be calculated for a non-zero temperature T, as[1]:

$$\alpha_{\mathrm{FCDW}}(T) = \exp\left\{-\sum_i \frac{S_i}{\hbar\Omega_i}\coth\frac{\hbar\Omega_i}{2k_{\mathrm{B}}T}\right\},$$

where the sums run over all modes, intramolecular and lattice phonons. The very fast decay with temperature of this factor explains why the ZPL can only observed at liquid-helium temperatures in molecular materials, whose vibrations frequencies are low compared to many inorganic materials.

7A.2 Methods section

7A.2.1 Experimental details

The hBN was obtained from two manufacturers: the company HQ-Graphene and the NIMS research institute[2]. Flakes of hBN were retrieved from a single crystal and deposited on a Si/SiO_2 substrate (University Wafer) through the exfoliation method using scotch tape. After exfoliation, the substrates were annealed in a tube oven (Thermcraft) at 750 ˚C for 12 hours in a moderate vacuum (rough pumping) and in the presence of oxygen. Subsequently, some terrylene was deposited on the annealed flakes by sublimation in a vacuum sublimation apparatus. These samples were loaded into the cryostat (Janis SVT-200-5) for measurement. After cooldown with liquid helium, the emission spectra were recorded upon excitation with a laser at 532 nm (Sprout-G15W, Lighthouse Photonics) in a confocal setup equipped with a Horiba IHR-320 spectrometer.

7A.2.2 Computational details

All periodic density functional theory (DFT) based geometry optimizations and molecular dynamics simulations were performed within the CP2K.8.2 software package.[3] The electron density was expanded in a hybrid Gaussian and plane wave scheme as is implemented in the Quickstep module within CP2K.8.2.[4] The boron valence electrons were described by the DZVP-MOLOPT-SR-GTH basis

set, while the DZVP-MOLOPT-GTH basis set was used for all other atoms.[5] The atom-centered basis set was augmented with plane waves up to a kinetic energy cutoff of 500 Ry. The Brillouin zone was integrated over the Γ-point only. The core electrons were modeled with the PBE-optimized, norm-conserving pseudopotentials developed by Goedecker, Teter and Hutter.[6–8] During the geometry optimizations, the electronic structure was consistently converged to a value of 10^{-7} a.u. Geometry optimizations were carried out with the conjugated gradients algorithm until a precision of 10^{-5} Ha $Bohr^{-1}$ and 10^{-4} $Bohr^{-1}$ was reached in the root mean squared change of the forces and geometry step size, respectively. The electron density was integrated over a multigrid of size 5. The calculations discussed in the main paper employ the screened hybrid-density functional introduced by Heyd, Scuseria and Ernzerhof (referred to as the HSE06 functional),[9–12] in combination with Grimme's third generation of atom pairwise dispersion corrections with Becke-Johnson damping (D3(BJ)) and a 22 Å cutoff.[13–15] The Hartree-Fock exchange was computed in an auxiliary density matrix using the AUX_FIT cFIT3 basis for all elements.[16]

The employed exchange-correlation functional plus dispersion correction setup has been used successfully in literature to study the electronic structure of polycyclic aromatic hydrocarbons adsorbed on hBN.[17] To assess the effect of the functional and dispersion corrections on the terrylene adsorption distance, additional calculations were performed with the GGA-PBE functional, the hybrid-B3LYP functional and the non-local dispersion-corrected rVV10 functional. The terrylene-hBN adsorption distances, calculated with these functionals are provided in Table 7A.1. These calculations were all performed in a periodic unit cell which was optimized at the PBE level. This PBE optimization resulted in a lattice parameter of 2.51 Å, which is very close to the experimentally observed lattice parameter of 2.50 Å. It was found that the HSE06 functional produces a terrylene-hBN distance in line with other calculations, while producing a more accurate band gap for hBN. Therefore, this functional plus dispersion correction was employed for the calculations in the main paper. Subsequently, also the cell-

optimization was performed again at this level of theory, yielding the correct lattice parameter of 2.50 Å.

Molecular dynamics (MD) simulations were performed at the same level of theory as the geometry optimizations with the PBE functional. However, the plane-wave cutoff was lowered to 400 Ry to speed up the calculations. The MD simulations employed a 0.5 fs timestep and were performed within the NVT ensemble by means of the Canonical Sampling Through Velocity Rescaling (CSVR) thermostat with a time constant of 20 fs for equilibration and 150 fs for production runs.[18]

***Table 7A.1**. Interplanar terrylene-hBN distance calculated with four different functionals plus dispersion corrections.*

	PBE + D3	B3LYP + D3BJ	HSE06 + D3BJ*	rVV10
Terrylene-hBN distance (Å)	3.34	3.21	3.25	3.31

* Cell optimization was performed also at this level of theory. Other calculations used the cell optimized at the PBE+D3 level.

The vibrationally resolved fluorescence spectra were calculated with the FCclasses program,[19] within the framework of the adiabatic Hessian approximation. The nuclear dependence of the electronic transition dipole is described in constant terms according to the Franck-Condon approximation. As input for the FCclasses program, ground and excited state optimized structures and Hessians, as well as transition dipole moments, were calculated with the Gaussian16.02 software.[20] The terrylene-hBN interface was described using a two-layer ONIOM procedure,[21,22] in which the terrylene was modeled at the DFT level, while the hBN electronic structure was described at the PM3 semi-empirical level.[23] Time-dependent DFT (TDDFT) was employed for the excited state

calculations on terrylene. The high level ONIOM layer utilized the B3LYP exchange correlation functional, expanded in a 6-31G(d,p) basis set.[24–27] Again, the D3BJ corrections were included to improve the description of dispersion forces. Notably, a very similar setup has been used in literature to interpret the vibronic spectrum of terrylene in naphthalene crystals.[28] Both ground and excited state ONIOM-based structure optimizations were initiated from the ground state optimized structures, extracted from the previously described periodic DFT calculations. During the ONIOM calculations, the PM3 level hBN layer was constrained except for a set of newly introduced hydrogen atoms, which were added manually to saturate the terminal N and B atoms.

7A.3 Computational workflow

A two-dimensional, single layer of hBN was optimized in a hexagonal periodic unit cell containing 9 x 9 boron nitride units, amounting to a total of 81 boron and 81 nitrogen atoms. During this procedure, both the unit cell size and interatomic forces in the hBN lattice were relaxed, resulting in a hBN lattice constant of 2.50 Å and a B-N bond length of 1.44 Å. These values are within 0.004 Å agreement with X-ray data reported in literature.[29,30] The preoptimized terrylene molecule was subsequently placed in the unit cell, in a parallel alignment with the surface and an intermolecular distance of ~3.5 Å. The subsequent structure optimization involved only relaxation of the interatomic distances, while the cell dimensions were kept constant.

After optimization of terrylene on the perfect hBN surface, defects were introduced into the hBN monolayer. All single-atom defects were introduced by removing or substituting one atom underneath the adsorbed terrylene molecule and subsequently performing a geometry optimization of the whole terrylene-hBN interface. Separately, an optimization of the hBN monolayer without the terrylene molecule was also performed to calculate the adsorption energy.

The periodic full-DFT optimized ground-state structure of the terrylene-hBN interface was taken as input for the aperiodic ONIOM calculations, where the

boron and nitrogen atoms at the box edges were terminated with hydrogen atoms. As the previous full-DFT calculations revealed considerable charge transfer from the V_N and O_N to terrylene, the ONIOM calculations with these defects were initiated with the excess electron transferred from the low-level (PM3) hBN layer to the high-level (TD-DFT) terrylene layer. Similarly, calculations with the V_B vacancy were initiated with one electron transferred from the high level layer to the low level layer. We note here that the defect-induced charge transfer results in the ground and excited states of interest being doublet states. In the presence of defects, additional electronic excitations with very low oscillator strength ($f < 0.05$) appear between the relevant ground and excited states. Throughout this study, we consistently identified the excited state of interest by verifying that the excitation predominantly involved the HOMO to LUMO transition in terrylene, and that the oscillator strength remains large ($f \approx 0.8$). On the perfect monolayer, both the S_0 and S_1 states of terrylene molecules were found to adsorb to the hBN with a bond distance of 3.03 Å (see table 7A.3). This is slightly shorter than in the full-DFT calculation (3.25 Å, see table 7A.3), however, we do not expect that this will affect significantly the fluorescence spectrum. It is known that the wavenumbers for peaks further away from the 0-0 ZPL are increasingly overestimated.[31] Therefore, all the spectra have been corrected with a linear scaling function of the form $y = ax + b$, where the a and b parameters were fitted such that the spectrum of terrylene in vacuum reproduced accurately the peaks at 247 and 1817 cm^{-1} observed in the spectrum presented in Figure 7.1a. Fitting the spectrum for terrylene on pristine hBN yielded parameters of $a = 0.97655035$ and $b = 4.1319276$, which have subsequently also been used to scale all the other spectra.

Interestingly, transitions at 33 and 276 cm^{-1} are observed for terrylene in vacuum and are quenced for terrylene on hBN. These transitions are associated with a slow, out of plane torsional mode that is inhibited in the adsorbed system (Figure 7A.6, mode 2). Some of the experimental single-molecule fluorescence spectra

show lines in the same region (see for instance, Figure 7.1, molecule A, line at 281 cm^{-1}).

7A.4 Additional results of the quantum chemical calculations

To assess the charge transfer from hBN to terrylene in the presence of different defects, we calculated the partial charge on terrylene by summing the partial charges of all atoms belonging to terrylene. We have performed this analysis with Mulliken charges, Hirshfeld charges and charges obtained from the Intrinsic Atomic Orbital Analysis (IOA).[32] The obtained values are provided in Table 7A.2. All three analysis methods produce overall the same trend in charge transfer from hBN to terrylene. Only an almost rigid shift in the absolute values is observed from one method to another.

***Table 7A.2**: Partial charges on terrylene calculated with different charge analysis methods.*

Defect site	Mulliken charge on Terrylene (e^- units)	IOA charges on Terrylene (e^- units)	Hirshfeld charge on Terrylene (e^- units)
Pristine hBN	0.02	0.16	0.30
O_N defect	−0.70	−0.59	−0.36
O_B defect	0.01	0.14	0.32
V_N vacancy	−0.68	−0.57	−0.36
V_B vacancy	0.83	1.06	1.11
V_{BN} vacancy	0.02	0.16	0.29

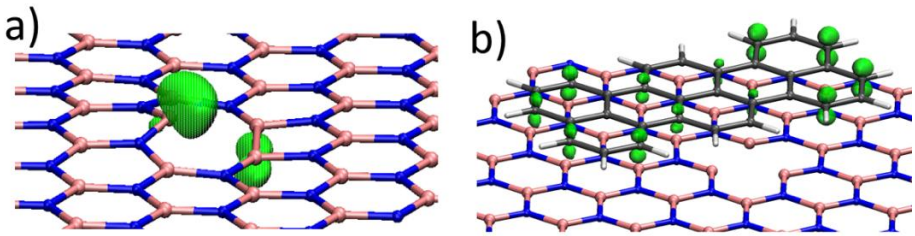

***Figure 7A.2**. Spin density of hBN with V_N vacancy (a) and spin density of terrylene chemisorbed at the V_N vacancy (b). Isosurfaces are plotted at 0.01 a.u.*

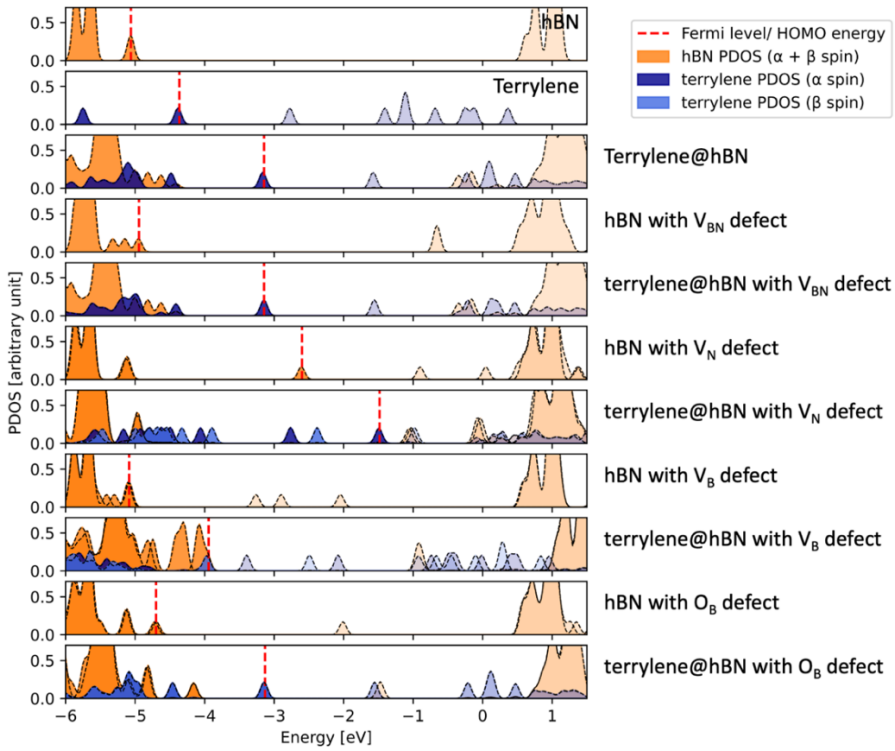

Figure 7A.3. *Projected density of states (PDOS) of pristine hBN and hBN with the V_N, V_B, V_{BN}, O_B defects, with and without chemisorbed terrylene. The plotted density of states were computed in CP2K at the HSE06+D3(BJ)-level and include a Gaussian broadening of 0.05 eV. Bands with transparent colors correspond to unoccupied levels.*

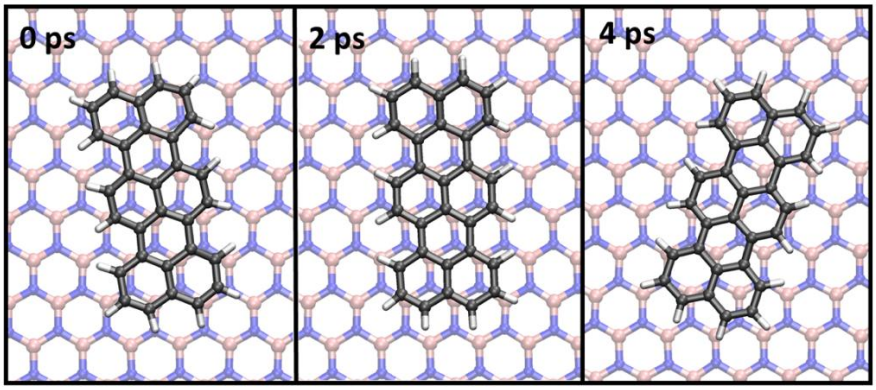

***Figure 7A.4**. Snapshots from a DFT-based (PBE+D3(BJ)) molecular dynamics trajectory of terrylene on pristine hBN. The simulation was performed at 300 K. Snapshots are taken at 0, 2 and 4 ps after the start of the production run and show that the terrylene molecule is free to diffuse over the surface.*

Table 7A.3. Terrylene-hBN distances (Å), calculated with full-DFT (HSE06+D3BJ) and with the ONIOM(B3LYP+D3BJ/PM3) approach in the ground and excited states.

	HSE06+D3BJ ground state	ONIOM (B3LYP+D3BJ/PM3) ground state	ONIOM (B3LYP+D3BJ/PM3) excited state
hBN	3.25	3.03	3.03
V_N	3.03	3.00	3.00
V_B	3.20	3.04	3.04
O_N	3.03	3.01	3.01

Table 7A.4. Interpretation of the simulated vibrationally resolved fluorescence spectrum for D_{2h} terrylene in vacuum.

hv **(cm^{-1})**	***hv*** **(cm^{-1})[a]**	**Intensity (a.u.)**	**Assignment**	**Symmetry**
0.0	0.0	1.000	0-0 ZPL	
26.6	30.1	0.026	1^2	Ag (Au^2)
30.1	33.5	0.047	2^2	Ag ($B1g^2$)
248.7	247.0	0.348	11^1	Ag
497.4	489.8	0.060	11^2	Ag
549.2	540.4	0.053	28^1	Ag
593.8	583.0	0.033	33^1	Ag
797.9	783.3	0.018	28^1, 11^1	Ag
842.5	826.9	0.012	33^1, 28^1	Ag
1313.4	1286.7	0.104	86^1	Ag
1348.0	1320.5	0.069	91^1	Ag
1396.4	1367.8	0.023	94^1	Ag
1407.6	1378.7	0.046	96^1	Ag
1562.1	1529.6	0.034	86^1, 11^1	Ag
1596.7	1563.3	0.024	91^1, 11^1	Ag
1608.2	1575.2	0.118	108^1	Ag
1656.3	1621.6	0.015	96^1, 11^1	Ag
1856.4	1818.0	0.039	108^1, 11^1	Ag
2922.2	2857.8	0.011	108^1, 86^1	Ag

[a] scaled with parameters (*a*, *b*): [0.97655035 4.1319276]

Table 7A.5. Interpretation of the simulated vibrationally resolved fluorescence spectrum for D_{2h} terrylene on hBN.

$h\nu$ (cm^{-1})	$h\nu$ (cm^{-1})[a]	Intensity (a.u.)	Assignment	Symmetry
0.0	0.0	1.000	0-0 ZPL	
249.3	247.6	0.346	17^1	Ag
498.6	491.0	0.059	17^2	Ag
549.9	541.2	0.052	34^1	Ag
594.3	584.5	0.034	39^1	Ag
799.2	784.6	0.018	34^1, 17^1	Ag
843.6	827.9	0.012	39^1, 17^1	Ag
1310.0	1284.4	0.111	92^1	Ag
1345.2	1317.8	0.077	97^1	Ag
1390.4	1361.9	0.021	100^1	Ag
1402.2	1373.5	0.043	101^1	Ag
1559.0	1526.9	0.036	92^1, 17^1	Ag
1594.5	1561.2	0.024	97^1, 17^1	Ag
1603.2	1569.8	0.118	114^1	Ag
1651.5	1616.9	0.014	101^1, 17^1	Ag
1852.5	1813.2	0.037	114^1, 17^1	Ag
2913.3	2849.1	0.012	114^1, 92^1	Ag

[a] scaled with parameters (*a*, *b*): [0.97655035 4.1319276]

Table 7A.6. Interpretation of the simulated vibrationally resolved fluorescence spectrum for D_{2h} terrylene on hBN + O_N defect.

$h\nu$ (cm^{-1})	$h\nu$ (cm^{-1})[a]	Intensity (a.u.)	Assignment	Symmetry
0.0	0.0	1.000	0-0 ZPL	
248.3	246.6	0.068	17^1	Ag
552.7	543.9	0.030	34^1	Ag
594.4	584.6	0.006	39^1	Ag
1362.1	1334.3	0.009	97^1	Ag
1387.9	1359.5	0.020	100^1	Ag
1431.3	1401.9	0.012	103^1	Ag
1622.9	1589.0	0.029	113^1	Ag
1731.0	1694.5	0.007	119^1	Ag
3504.03	3426.0	0.010	121^2	Ag ($B1g^2$)

[a] scaled with parameters (*a*, *b*): [0.97655035 4.1319276]

Table 7A.7. Interpretation of the simulated vibrationally resolved fluorescence spectrum for D_{2h} terrylene on hBN + V_N vacancy.

hv **(cm^{-1})**	***hv*** **(cm^{-1})[a]**	**Intensity (a.u.)**	**Assignment**	**Symmetry**
0.0	0.0	1.000	0-0 ZPL	
248.4	246.7	0.069	17^1	Ag
552.7	543.9	0.030	34^1	Ag
594.3	584.5	0.008	39^1	Ag
1362.1	1334.3	0.008	97^1	Ag
1388.9	1360.5	0.019	100^1	Ag
1431.4	1402.0	0.013	103^1	Ag
1624.1	1590.2	0.030	113^1	Ag
1731.2	1694.8	0.008	119^1	Ag
2310.1	2260.0	0.005	121^1, 35^1	Ag (B1g*B1g)
2933.6	2869.0	0.005	121^1, 84^1	Ag (B1g*B1g)
3504.4		0.012	121^2	Ag ($B1g^2$)

[a] scaled with parameters (*a*, *b*): [0.97655035 4.1319276]

Table 7A.8. Interpretation of the simulated vibrationally resolved fluorescence spectrum for D_{2h} terrylene on hBN + V_B vacancy.

hν (cm^{-1})	hν (cm^{-1})[a]	Intensity (a.u.)	Assignment	Symmetry
0.0	0.0	1.000	0-0 ZPL	
250.4	248.6	0.050	17^1	Ag
557.2	548.3	0.018	34^1	Ag
601.1	591.2	0.014	39^1	Ag
1380.1	1351.8	0.006	96^1	Ag
1414.3	1385.3	0.024	100^1	Ag
1455.2	1425.2	0.011	103^1	Ag
1643.0	1608.6	0.026	113^1	Ag
1661.6	1626.8	0.019	55^2	Ag ($B3u^2$)
1734.8	1698.2	0.007	119^1	Ag
2258.2	2209.4	0.008	101^1, 55^1	Ag (B3u*B3u)
2274.4	2225.2	0.032	102^1, 55^1	Ag (B3u*B3u)
2553.7	2497.9	0.017	117^1, 55^1	Ag (B3u*B3u)
2871.0	2807.8	0.016	102^1, 101^1	Ag (B3u*B3u)
2887.2	2823.6	0.007	102^1	Ag ($B3u^2$)
3150.3	3080.5	0.006	117^1, 101^1	Ag (B3u*B3u)
3166.4	3096.3	0.017	117^1, 102^1	Ag (B3u*B3u)

[a] scaled with parameters (*a*, *b*): [0.97655035 4.1319276]

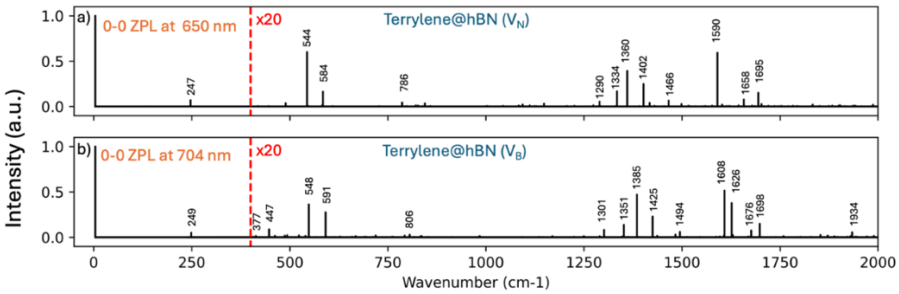

***Figure 7A.5**. Computed vibrationally resolved fluorescence spectra of terrylene on the V_N defect (a), and on the V_B defect (b). Both spectra are shifted such that their respective 0-0 ZPL is centered at 0. The spectra are corrected with a linear scaling function with parameters 0.977 and 4.132, as suggested by Palafox.*[31] *All intensities are scaled such that the intensity of the 0-0 ZPL is 1. The intensities of the peaks observed above 400 cm^{-1} are multiplied by a factor 20.*

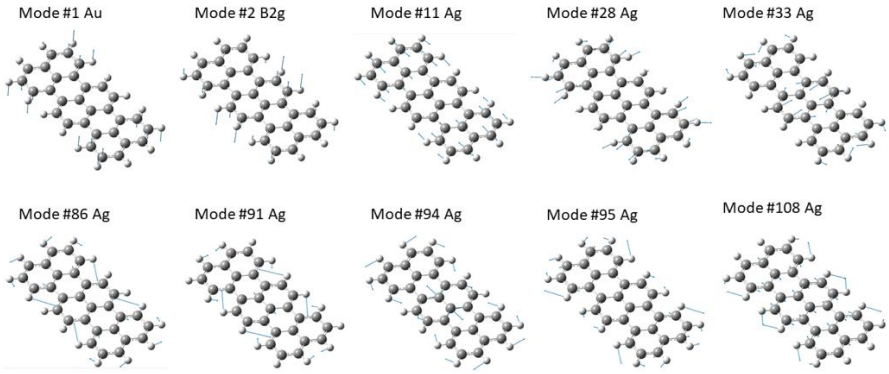

***Figure 7A.6**. Visualization of the most prominent vibrational modes observed in the $S_1 \rightarrow S_0$ vibrationally resolved fluorescence spectrum for terrylene in vacuum.*

7A.5 References

[1] K. K. Rebane, *Impurity Spectra of Solids*, Plenum New York, **1970**.
[2] K. Watanabe, T. Taniguchi, H. Kanda, *Nat. Mater.* **2004**, *3*, 404–409.
[3] T. D. Kühne, M. Iannuzzi, M. Del Ben, V. V. Rybkin, P. Seewald, F. Stein, T. Laino, R. Z. Khaliullin, O. Schütt, F. Schiffmann, D. Golze, J. Wilhelm, S. Chulkov, M. H. Bani-Hashemian, V. Weber, U. Borštnik, M. Taillefumier, A. S. Jakobovits, A. Lazzaro, H. Pabst, T. Müller, R. Schade, M. Guidon, S. Andermatt, N. Holmberg, G. K. Schenter, A. Hehn, A. Bussy, F. Belleflamme, G. Tabacchi, A. Glöß, M. Lass, I. Bethune, C. J. Mundy, C. Plessl, M. Watkins, J. VandeVondele, M. Krack, J. Hutter, *J. Chem. Phys.* **2020**, *152*, 194103.
[4] J. VandeVondele, M. Krack, F. Mohamed, M. Parrinello, T. Chassaing, J. Hutter, *Comput. Phys. Commun.* **2005**, *167*, 103–128.
[5] J. VandeVondele, J. Hutter, *J. Chem. Phys.* **2007**, *127*, 114105.
[6] S. Goedecker, M. Teter, J. Hutter, *Phys. Rev. B* **1996**, *54*, 1703–1710.
[7] C. Hartwigsen, S. Goedecker, J. Hutter, *Phys. Rev. B* **1998**, *58*, 3641–3662.
[8] M. Krack, *Theor. Chem. Acc.* **2005**, *114*, 145–152.
[9] J. Heyd, G. E. Scuseria, M. Ernzerhof, *J. Chem. Phys.* **2003**, *118*, 8207–8215.
[10] J. Heyd, G. E. Scuseria, *J. Chem. Phys.* **2004**, *121*, 1187–1192.
[11] J. Heyd, J. E. Peralta, G. E. Scuseria, R. L. Martin, *J. Chem. Phys.* **2005**, *123*, 174101.
[12] J. Heyd, G. E. Scuseria, M. Ernzerhof, *J. Chem. Phys.* **2006**, *124*, 219906.
[13] S. Grimme, *J. Comput. Chem.* **2004**, *25*, 1463–1473.
[14] S. Grimme, *Wiley Interdiscipl. Rev.: Comput.l Mol. Sci.* **2011**, *1*, 211–228.
[15] S. Grimme, S. Ehrlich, L. Goerigk, *J. Comput. Chem.* **2011**, *32*, 1456–1465.
[16] M. Guidon, J. Hutter, J. VandeVondele, *J. Chem. Theory Comput.* **2010**, *6*, 2348–2364.
[17] G. Melani, J. P. Guerrero-Felipe, A. M. Valencia, J. Krumland, C. Cocchi, M. Iannuzzi, *Phys. Chem. Chem. Phys.* **2022**, *24*, 16671–16679.
[18] G. Bussi, D. Donadio, M. Parrinello, *J. Chem. Phys.* **2007**, *126*, 014101.
[19] J. Cerezo, F. Santoro, *J. Comput. Chem.* **2023**, *44*, 626–643.
[20] M. J. Frisch, G. W. Trucks, H. B. Schlegel G. E. Scuseria, M. A. Robb, J. R. Cheeseman, G. Scalmani, V. Barone, G. A. Petersson, H. Nakatsuji, X. Li, M. Caricato, A. V. Marenich, J. Bloino, B. G. Janesko, R. Gomperts, B. Mennucci, Gaussian 16; Gaussian, Inc.: Wallingford, CT, **2016.**
[21] S. Dapprich, I. Komaromi, K. S. Byun, K. Morokuma, M. J. Frisch, *J. Mol. Struct. THEOCHEM*, **1999**, 461-462, 1-21.
[22] L. W. Chung, W. M. C. Sameera, R. Ramozzi, A. J. Page, M. Hatanaka, G. P. Petrova, T. V. Harris, X. Li, Z. Ke, F. Liu, H.-B. Li, L. Ding, K. Morokuma, *Chem. Rev.* **2015**, *115*, 5678–5796.
[23] J. J. P. Stewart, *J. Mol. Model.* **2007**, *13*, 1173–1213.
[24] A. D. Becke, *Phys. Rev. A.* **1988**, *38*, 3098.
[25] A. D. Becke, *J. Chem. Phys.* **1993**, *98*, 1372–1377.
[26] S. H. Vosko, L. Wilk, M. Nusair, *Can. J. Phys.* **1980**, *58*, 1200–1211.
[27] P. J. Stephen, F. J. Devlin, C. F. Chabalowski, M. J. Frisch, *J. Phys. Chem.* **1994**, *98*, 11623–11627.
[28] I. Deperasińska, B. Kozankiewicz, *Chem. Phys. Lett.* **2017**, *684*, 208–211.
[29] R. W. Lynch, H. G. Drickamer, *J. Chem. Phys.* **1966**, *44*, 181–184.
[30] E. K. Sichel, R. E. Miller, M. S. Abrahams, C. J. Buiocchi, *Phys. Rev. B* **1976**, *13*, 4607–4611.
[31] M. A. Palafox, *Phys. Sci. Rev.* **2018**, *3*, 20170184.
[32] G. Knizia, *J. Chem. Theory Comput.* **2013**, *9*, 4834–4843

.